*J. Fluid Mech.* (2001), *vol.* 426, *pp.* 47–72. Printed in the United Kingdom

© 2001 Cambridge University Press

# Flow at the interface of a model fibrous porous medium

By DAVID F. JAMES[1] AND ANTHONY M. J. DAVIS[2]

[1]Department of Mechanical and Industrial Engineering, University of Toronto, Toronto, Canada M5S 3G8

[2]Department of Mathematics, University of Alabama, Tuscaloosa, AL 35487-0350, USA

(Received 7 June 1999 and in revised form 16 June 2000)

Planar flow in the interfacial region of an open porous medium is investigated by finding solutions for Stokes flow in a channel partially filled with an array of circular cylinders beside one wall. The cylinders are in a square array oriented across the flow and are widely spaced, so that the solid volume fraction $\phi$ is 0.1 or less. For this spacing, singularity methods are appropriate and so they are used to find solutions for both planar Couette flow and Poiseuille flow in the open portion of the channel. The solutions, accurate to $O(\phi)$, are used to calculate the apparent slip velocity at the interface, $U_s$, and results obtained for $U_s$ are presented in terms of a dimensionless slip velocity. For shear-driven flow, this dimensionless quantity is found to depend only weakly on $\phi$ and to be independent of the height of the array relative to the height of the channel and independent of the cylinder size relative to the height of the channel. For pressure-driven flow, $U_s$ is found to be less than that under comparable shear-flow conditions, and dependent on cylinder size and filling fraction in this case. Calculations also show that the external flow penetrates the porous medium very little, even for sparse arrays, and that $U_s$ is about one quarter of the velocity predicted by the Brinkman model.

## 1. Introduction

When a fluid flows through a channel bounded by a porous medium, or flows around a porous body, the no-slip condition at the surface of the porous medium generally does not apply. There is effectively a slip velocity at the surface, and studies of interfacial flow have focused on the dependence of this velocity on the characteristics of the medium and the external flow. But only a few such studies have been done and so it is not known how to prescribe the velocity at the boundary for an arbitrary situation. The flow may be driven by shear or pressure, and the basic situation is shear flow over and through a semi-infinite porous medium adjacent to a channel, as sketched in figure 1. The flow is driven by the other wall of the channel (not seen in the figure) moving at a constant velocity and generating planar shear flow in the channel. Figure 1 illustrates the general velocity profile: away from the interface the velocity becomes linear in the channel and inside the porous medium the velocity decays to zero. The quantities of particular interest are the velocity at the interface, the so-called slip velocity, and the penetration of flow into the porous medium.

When flow in the channel is driven by pressure instead of shear, the velocity profile away from the interface becomes parabolic while inside the porous medium

https://doi.org/10.1017/S0022112000002160 Published online by Cambridge University Press

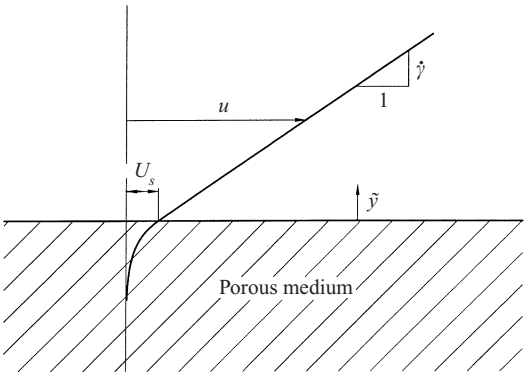



FIGURE 1. The velocity profile for parallel flow over and through a porous medium. The flow is driven by shear, created by an unseen moving wall parallel with and above the interface. The streamwise velocity $u$ decreases from linear in the channel (shear rate $\dot{\gamma}$) to zero in the medium. The slip velocity at the interface is designated $U_s$.

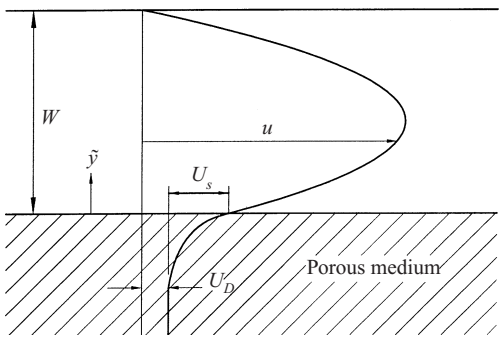



FIGURE 2. The velocity profile for pressure-driven planar flow in a channel and in the adjacent porous medium. The velocity deep in the medium is $U_D$, as given by Darcy's law, and the velocity at the interface is the sum of $U_D$ and the slip velocity $U_s$.

the velocity is constant, as indicated in figure 2. Hence it appears that two different cases need to be considered: shear-driven and pressure-driven flows. However, for a pressure-driven flow, the velocity close to the interface is linear or nearly linear, similar to the shear-driven case. Hence the flow just outside the porous medium appears to be the same for both cases, i.e. linear shear flow. Both cases will be discussed in more detail in a later section, and the results of our work will eventually show just how closely the two cases are related. For the moment, though, we take the approach that shear-driven flow is the more basic flow, with possible modification when the flow is pressure-driven.

In both figures 1 and 2, the slip velocity is denoted by $U_s$. This velocity is unambiguous in the former but not in the latter. That is, in the pressure-driven case, there is a uniform velocity in the porous medium, the drift velocity $U_D$, and the velocity at the interface is the sum of $U_s$ and $U_D$. The sum has been termed the slip velocity by some authors, following Beavers & Joseph (1967), but it seems more logical to distinguish between the velocity caused by penetration of the external flow and the velocity caused by the pressure gradient in the porous medium. That distinction is made here. By associating $U_s$ with penetration of the outer flow, figures

https://doi.org/10.1017/S0022112000002160 Published online by Cambridge University Press

1 and 2 are consistent and it will be straightforward later to make comparisons of results from the two cases.

The slip velocity is of little interest when it is small. For a porous medium made of compacted particles, resistance to flow in the material is so large that the slip velocity is small and there is little penetration. Flow penetrates the medium only when its solid volume fraction, $\phi$, is low, generally less than about 0.1. A volume fraction in this range is possible only if the medium is made of fibres or fibre-like particles, because a firm structure cannot be formed otherwise. When $\phi$ is in the range of 0.1 and less, interfibre distances are large and there is considerable open space. For example, when $\phi$ is 0.1 and the fibres are evenly spaced, the distance between fibres is about three times the fibre cross-dimension. With this spacing, the external flow can easily penetrate the structure. While fibrous media generally have $\phi$ values around 0.1, values may be as low as 0.005, as the data collected by Jackson & James (1986) show. Values below 0.005 are possible, but only when the fibres are polymer chains in solution. In this situation, the entangled chains form a porous medium whose shape is maintained by diffusive forces (Brownian motion) or by electrostatic charges along the chains. Such a situation occurs, for example, when polymer chains are attached to a surface and extend outward because the fluid flowing over the surface is a solvent of the polymer. To sum up, the relevant porous media are necessarily fibrous, and the media range from polymer chains in solution to filters and insulation.

### 1.1. *Dimensional reasoning*

(i) Shear-driven flow

In studying flow in the interfacial region, it is useful to review what dimensional reasoning reveals about the situation. For shear-driven flow, the external flow is specified by the shear rate $\dot{\gamma}$. Fluid density is not considered a factor because velocities and pore dimensions in practical situations are so small that Reynolds numbers are ordinarily much less than unity. Hence the only relevant fluid parameter is the viscosity. In characterizing the porous medium, it is assumed for the moment that the only necessary parameter is the permeability $k$, as it appears in Darcy's law for uniform flow. While this is a reasonable assumption for a general porous medium, it may not be appropriate for a medium which is described by two or more length scales. This assumption will be addressed later because the media studied here have in fact two length scales, and so the development here is based on the assumption that the single most important length scale, $\sqrt{k}$, is sufficient. But when the flow is shear flow, as in the present case, flow resistance probably depends not only on $k$ but also on the geometrical details of the medium.

The above parameters influence how the velocity $u$ depends on the transverse distance $\tilde{y}$, i.e. the general relation for $u$ is

$$u = \mathscr{F}(\tilde{y}, k, \dot{\gamma}, \text{geometry}), \tag{1}$$

where $\mathscr{F}$ means 'some function of', where $u$ is spatially-averaged where necessary, and where $\tilde{y}$ is measured from the interface, positive in the direction of the channel. Viscosity is not included as a variable because there are no other dynamical quantities. By dimensional analysis, this equation reduces to

$$\frac{u}{\dot{\gamma}\sqrt{k}} = \mathscr{F}\left(\frac{\tilde{y}}{\sqrt{k}}, \text{geometry}\right). \tag{2}$$

https://doi.org/10.1017/S0022112000002160 Published online by Cambridge University Press

The interfacial (slip) velocity $U_s \equiv u(0)$ is therefore

$$U_s = \dot{\gamma}\sqrt{k} f_1, \tag{3}$$

where $f_1$ is a function of geometry only.

The above equation is not in the form of a boundary condition, but it can be made into one by considering the velocity gradient, $\mathrm{d}u/\mathrm{d}\tilde{y}$. By differentiating $u$ or by dimensional reasoning, the gradient is

$$\frac{\mathrm{d}u}{\mathrm{d}\tilde{y}} = \dot{\gamma}\mathscr{F}\left(\frac{\tilde{y}}{\sqrt{k}}, \text{geometry}\right), \tag{4}$$

where $\mathscr{F}$ continues to denote a general function of its independent variables, and is different from the general functions in (1) and (2). At the wall,

$$\frac{\mathrm{d}u}{\mathrm{d}\tilde{y}}(0) = \dot{\gamma} f_2, \tag{5}$$

where $f_2$ is another function of geometry. The shear rate $\dot{\gamma}$ can be eliminated by combining this relation with (3) to yield

$$\frac{\mathrm{d}u}{\mathrm{d}\tilde{y}}(0) - \frac{f_2}{f_1\sqrt{k}}u(0) = 0. \tag{6}$$

Hence the boundary condition on $u$ at the interface is homogeneous.

(ii) Pressure-driven flow

Now consider the situation when the flow is driven by a pressure gradient and not by a moving wall, as illustrated in figure 2. In this case, $\partial p/\partial\tilde{y} = 0$ and, for a gradient of $G(= -\mathrm{d}p/\mathrm{d}x)$, the velocity in the channel is, using the coordinate system of figure 2,

$$u(\tilde{y}) = \frac{G(\tilde{y}W - \tilde{y}^2)}{2\mu} + U_s\left(1 - \frac{\tilde{y}}{W}\right), \tag{7}$$

where $W$ is the channel width and $\mu$ is the viscosity. The shear rate at the interface, $\dot{\gamma}_w$, is

$$\dot{\gamma}_w = \frac{\mathrm{d}u}{\mathrm{d}\tilde{y}}(0) = \frac{GW}{2\mu} - \frac{U_s}{W}. \tag{8}$$

The interfacial shear rate depends on the the first term alone if the slip velocity is small enough, that is,

$$\dot{\gamma}_w \simeq \frac{GW}{2\mu} \quad \text{if} \quad U_s \ll \frac{GW^2}{2\mu}. \tag{9}$$

Since $GW^2/8\mu$ is approximately $U_{max}$, the maximum velocity in the channel, the condition under which the interfacial shear rate $\dot{\gamma}$ is approximated well by the wall shear rate $GW/2\mu$ is

$$U_s \ll 4U_{max}. \tag{10}$$

This condition is easily met. Later work will show that $U_s$ is less than 5% of $U_{max}$ for practical situations and no more than 20% for the most extreme situations. In the latter cases, the approximation (10) is accurate to 5% and so the approximation is appropriate in general.

Dimensional reasoning is now applied to pressure-driven flows. In these cases the velocity depends on $G$ and so one of the independent variables is a dynamical quantity, in contrast to the purely kinematical situation when the flow is shear-driven.

https://doi.org/10.1017/S0022112000002160 Published online by Cambridge University Press

For dimensional consistency, a second dynamical variable must be introduced, which is $\mu$. The general relation for $u$ is thus

$$u = \mathscr{F}(\tilde{y}, k, G, \mu, W, \text{geometry}). \tag{11}$$

In forming a dimensionless equation, the length scale is chosen to be $\sqrt{k}$ because it is far more important than the alternative, $W$. A natural dimensionless formulation is

$$\frac{u\mu}{Gk} = \mathscr{F}\left(\frac{\tilde{y}}{\sqrt{k}}, \frac{W}{\sqrt{k}}, \text{geometry}\right). \tag{12}$$

Equation (9) shows that $G/\mu$ is approximated well by $2\dot{\gamma}_w/W$, and so the dynamical variable $G$ can be eliminated from (12) to produce a relation which is purely kinematical. If the focus is again on the interfacial region and if the flow there is characterized by the shear rate $\dot{\gamma}_w$, then the distance to the far wall, $W$, is no longer relevant. More particularly, if $W$ is many times $\sqrt{k}$, which is normally the case, then the far wall should not be a factor and flow at the interface should depend only on the local flow conditions, i.e. on the linear portion of the parabolic profile. When $W$ is not a factor, therefore, (12) reduces to

$$\frac{u}{\dot{\gamma}_w\sqrt{k}} = \mathscr{F}\left(\frac{\tilde{y}}{\sqrt{k}}, \text{geometry}\right), \tag{13}$$

which has the same form as the shear-driven case, i.e. as equation (2). Consequently, the velocity profile for a pressure-driven flow should have the same interfacial features as those in the equivalent shear-driven flow when $W$ is much greater than $\sqrt{k}$.

### 1.2. *The slip coefficient*

In their landmark work, Beavers & Joseph (1967) investigated slip at the interface for pressure-driven flow and proposed the following equation as the flow condition at the interface:

$$\frac{\mathrm{d}u}{\mathrm{d}\tilde{y}}(0) = \frac{\alpha}{\sqrt{k}}(U_s - U_D), \tag{14}$$

where $U_s$ in this case refers to the total velocity at the interface and $\alpha$ is the so-called 'slip coefficient'. This equation is equivalent to (6), which applies to shear-driven flow. But it also applies to pressure-driven flow when $W \gg \sqrt{k}$, as shown by the preceding paragraph and (13). The equivalence of (14) with (6) shows that $\alpha$ is equal to $f_2/f_1$; since $f_1$ and $f_2$ are functions of geometry only, $\alpha$ should also depend only on geometry.

Beavers & Joseph conducted experiments with several 'natural' porous media – foametals and axolites (compact granular materials) – to determine values of $\alpha$. Their experiments yielded an $\alpha$ value of 0.1 for two axolites and values of 0.8, 1.5 and 4 for three foametals. This range demonstrates that geometry is important at the interface, even though it is a secondary parameter in the bulk of the medium. Other studies have generated further values of $\alpha$. Taylor (1971) analysed flow past a model porous medium – a plate with deep rectangular grooves aligned with the flow – and found that $\alpha$ has a minimum of 1.3 and increases to several times this value as the walls between the grooves become thinner. Another theoretical work in which values of $\alpha$ were found was the study by Sahraoui & Kaviany (1992). They used numerical techniques to investigate flow past arrays of circular cylinders and found that, for a square array, $\alpha$ increased from 1.2 to 4 as the porosity increased, i.e. $\alpha$ depends on more than geometry because the geometry is fixed with a square array. They also

https://doi.org/10.1017/S0022112000002160 Published online by Cambridge University Press

showed that $\alpha$ may be as low as 0.4 when cylinders on the outermost row are not aligned. Taken together, these prior works show that $\alpha$ is of order 1 and that it can vary by at least a factor of ten, depending on the geometry.

In these works, the interface was taken to be the flat or machined surface of the medium, or, in the case of arrays of cylinders, to be the plane tangent to the outer edges of the cylinders. A prior study in which the location of the interface was exterior to the medium was that by Sangani & Behl (1989), who investigated flow over semi-infinite periodic arrays of spheres. Using singular solutions of the Stokes and Laplace equations, they determined flow fields in the interfacial region and, for the chosen location of the interface, showed good agreement of the slip velocity with that predicted by Brinkman's equation. Since this equation is widely used when shear occurs in a porous medium, it is reviewed next.

### 1.3. *Brinkman's equation and penetration*

The equation developed by Brinkman (1947) is a combination of Stokes' equation and Darcy's law:

$$\nabla p = \mu^* \nabla^2 \boldsymbol{v} - \frac{\mu}{k}\boldsymbol{v}, \tag{15}$$

where $\nabla p$ is the pressure gradient, $\boldsymbol{v}$ is the velocity vector, $\mu$ is the viscosity and $\mu^*$ is the effective viscosity. Because the equation is second order in velocity, it can be matched to the second-order Stokes' equation for the external flow and consequently provides continuity of both stress and velocity at the interface. The equation has been rigorously derived, and the relation of the effective viscosity to the actual fluid viscosity has been investigated. The studies show that $\mu^*/\mu$ is generally greater than unity and, in the most authoritative of these, Kim & Russel (1985) establish that the ratio is $1 + 5\phi/2$ to order $\phi$. Since the present work will be related to Brinkman's equation, and since the range of $\phi$ in the present work is 0.001 to 0.1, the most appropriate value of $\mu^*$ in Brinkman's equation is $\mu$, with a possible modification after comparisons are made.

For the basic wall-driven flow in figure 1, the single-viscosity Brinkman equation reduces to

$$\frac{\mathrm{d}^2 u}{\mathrm{d}\tilde{y}^2} - \frac{1}{k}u = 0 \tag{16}$$

and the solution of this equation in the porous medium, i.e. for $\tilde{y} \leqslant 0$, is

$$u = U_s \, \mathrm{e}^{\tilde{y}/\sqrt{k}}. \tag{17}$$

This relation shows that the depth of penetration is of order $\sqrt{k}$, which in turn is of order of the pore size, particularly in a sparse medium. To better understand the relation between penetration and pore size, consider the simplest model of a sparse medium, a square array of parallel rods. For flow across the rods, the dependence of permeability on solidity is approximated well by

$$\frac{k}{a^2} \simeq \frac{1}{8\phi} \ln \frac{1}{\phi}, \tag{18}$$

where $a$ is the rod radius (see, for example, Jackson & James 1986). If $2L$ is the rod spacing, then $\phi = \pi a^2/4L^2$, and $\sqrt{k} = 0.6L$ when $\phi$ is 0.1. Under these conditions, the velocity at the second row of cylinders, where $\tilde{y} \simeq -2L$, is about 4% of its value at the interface.

Hence Brinkman's equation predicts that the depth of penetration is comparable

https://doi.org/10.1017/S0022112000002160 Published online by Cambridge University Press

with the pore size, and this result depends only weakly on $\phi$ because of the log term in (18). This relation of penetration to pore size is questionable, however, because Darcy's law is not appropriate at this scale. That is, this continuum equation is valid over distances much larger than $\sqrt{k}$, and not on the scale of $\sqrt{k}$ or the pore size. Although Brinkman's equation has been validated theoretically and appears to be accurate in some cases (e.g. Sangani & Behl 1989), it cannot be expected to be accurate in general nor to provide information about the flow field close to the interface. In fact, the most detailed knowledge about flow near the interface has come from numerical studies and results from these are not consistent with Brinkman's equation.

### 1.4. *Numerical studies*

The principal numerical studies are those of Larson & Higdon (1986, 1987). Their porous media are arrays of rods, primarily square arrays, aligned with and across the flow. In their studies, the pressure gradient is zero and the velocity profile is linear away from the interface. Their streamline patterns reveal eddies within the arrays when the flow is across the array, with eddy location depending on array geometry and $\phi$. The eddy motion is unexpected because Brinkman's equation predicts only positive values of the velocity.

In addition to finding streamline patterns revealing the circulation, Larson & Higdon calculated the slip velocity, which they took to be the average velocity along the line joining the rod centres. They used two methods to find this velocity, one based on flow rate in the channel and the other based on Brinkman's equation and flow rate in the porous medium. Calculated by either method, the slip velocity decreases with $\phi$ as expected, but some values are negative and the two sets of results differ by as much as 10 to 1 in magnitude. It is difficult to envisage a negative slip velocity, and their negative values are probably due to their method of calculation because their streamline patterns suggest positive velocities on the plane in question.

Another numerical investigation of flow across rod arrays was carried out by Sahraoui & Kaviany (1992). They found values of the slip coefficient for various rod arrangements, and these values show a strong dependence on rod configuration right at the interface. Even so, the values appear to have limited usefulness because they pertain to high values of $\phi$ – a minimum of 0.2, and 0.52 in many cases – and in this regime the slip velocity is zero for practical purposes. Consequently, numerical studies have revealed an unexpected circulation but have done little to improve our knowledge of the slip velocity.

### 1.5. *Objectives*

Even though the general features of interfacial flow are understood, further knowledge is needed about the slip velocity and the degree of penetration. While both are important and in fact related, the present work focuses on the velocity because it affects the flow rate in the channel.

The objective, then, is to find the slip velocity for a model porous medium. The selected model is an array of rods oriented across the flow because it is the most appropriate model at the low solid fractions necessary for discernible slip. This model is more suitable than, for example, an array of spheres because the latter cannot be realized physically. The choice of orientation is also governed by practicality. If the rod array were aligned with the flow, the problem would be easier to solve; but in fibrous materials the fibres are much more likely to be aligned across the flow and so that is the situation addressed here. For such problems, computational techniques are

https://doi.org/10.1017/S0022112000002160 Published online by Cambridge University Press

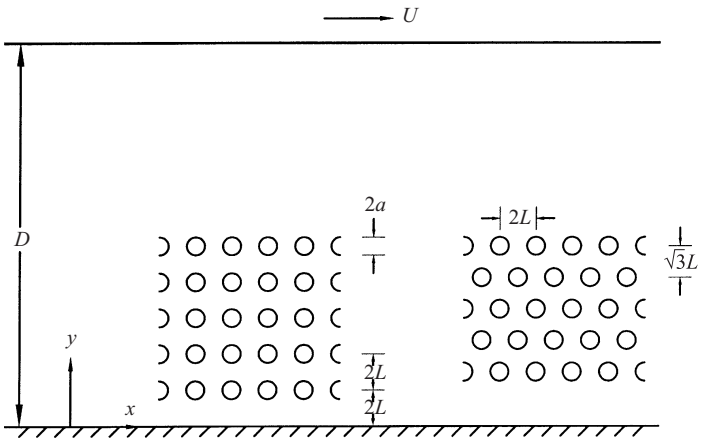



FIGURE 3. Square and equilateral arrays of cylinders partially filling a planar channel of total width $D$. The cylinder diameter is $2a$ and the distance between cylinders is $2L$. The flow is driven by the upper wall moving at a constant speed $U$.

the methods of choice these days, but the prior numerical studies have not yielded particularly useful results for the slip velocity. Because the rods must be widely spaced to generate a slip velocity of significance, analytical methods are also appropriate. Hence the plan is to use singularity methods to solve for the flow field, and from the solution to determine the slip velocity at the interface. The scope of the plan is to find this velocity for both shear-driven and pressure-driven flows, over a wide range in $\phi$, and for different array configurations.

## 2. Two-dimensional analysis for shear-driven flow

Consider a channel of width $D$ which is partially filled with an array of circular cylinders in rows parallel with the wall, as illustrated in figure 3. The array may be square or equilateral, as suggested in the figure, and the former is treated first. Steady two-dimensional creeping flow is generated by the uniform translation of the upper wall and disturbed by the presence of the small cylinders. Let Cartesian coordinates and corresponding unit vectors be defined so that the stationary wall is at $y = 0$ and the wall at $y = D$ moves with speed $U\hat{\boldsymbol{x}}$. Cylinders of radius $a$ are placed with their centres at $\{(2mL, 2nL); 1 \leqslant m \leqslant M, -\infty < n < \infty\}$, where $2ML < D$. The velocity field $\boldsymbol{v}(x, y)$ satisfies no-slip conditions at the walls and cylinder boundaries and the creeping flow equations

$$\mu\nabla^2\boldsymbol{v} = \nabla p, \qquad \nabla\cdot\boldsymbol{v} = 0, \tag{19}$$

where $\mu$ is the viscosity and $p$ the dynamic pressure. Equations (19) allow a stream function $\psi$ to be introduced such that

$$v_x = \frac{\partial\psi}{\partial y}, \qquad v_y = -\frac{\partial\psi}{\partial x}, \qquad \nabla^4\psi = 0. \tag{20}$$

The purpose of the following calculation is to construct an approximation to the velocity field $\boldsymbol{v}(x, y)$, evidently periodic in $x$ with period $2L$, that satisfies the no-slip conditions exactly on the channel walls and up to order $\phi$ on the cylinders, where the volume fraction $\phi$ is given by

$$\phi = \pi a^2/4L^2. \tag{21}$$

https://doi.org/10.1017/S0022112000002160 Published online by Cambridge University Press

### 2.1. *Point force arrays*

The stream function due to a point force $4\pi\mu\hat{\mathbf{x}}$ at $(x_0, y_0)$ is (e.g. Davis 1993)

$$\tfrac{1}{2}(y-y_0)\{1-\ln[(x-x_0)^2+(y-y_0)^2]\}.$$

Hence the stream function due to a periodic array of oppositely directed point force singularities at $\{(2lL, \pm y_0); -\infty < l < \infty\}$ in the presence of rigid walls at $y = 0, D$ is given by

$$\psi_2^\infty = -\tfrac{1}{2}(y-y_0)\ln\left[\cosh\frac{\pi(y-y_0)}{L}-\cos\frac{\pi x}{L}\right]+\tfrac{1}{2}(y+y_0)\ln\left[\cosh\frac{\pi(y+y_0)}{L}-\cos\frac{\pi x}{L}\right]$$

$$+\psi_0(y,y_0)+\sum_{s=1}^{\infty}\psi_s(y,y_0)\cos\frac{s\pi x}{L}, \tag{22}$$

in which the first term contains all the singularities and is obtained by Fourier transform methods and in which additional terms required to ensure no-slip at $y = 0, D$ are such that

$$\psi_s(y,y_0,D) = -\frac{2}{s}\left\{DH^*(ky,ky_0;kD)+\frac{\partial}{\partial k}\left[\mathrm{e}^{-kD}\frac{\cosh ky\sinh ky_0}{\sinh kD}\right]\right\}_{k=s\pi/L}, \tag{23a}$$

$$\frac{\mathrm{d}\psi_0}{\mathrm{d}y} = -\frac{2\pi y y_0}{LD}+\tfrac{1}{2}Gy(D-y). \tag{23b}$$

Here $G$ is set equal to zero to avoid introducing a pressure gradient and $H^*$ is related to the symmetric function

$$H = \frac{k}{2D}\left(\frac{\cosh kD+1}{\sinh kD-kD}\right)\frac{\partial}{\partial k}\left[\frac{\cosh k(\frac{1}{2}D-y)}{\cosh\frac{1}{2}kD}\right]\frac{\partial}{\partial k}\left[\frac{\cosh k(\frac{1}{2}D-y_0)}{\cosh\frac{1}{2}kD}\right]$$

$$+\frac{k}{2D}\left(\frac{\cosh kD-1}{\sinh kD+kD}\right)\frac{\partial}{\partial k}\left[\frac{\sinh k(\frac{1}{2}D-y)}{\sinh\frac{1}{2}kD}\right]\frac{\partial}{\partial k}\left[\frac{\sinh k(\frac{1}{2}D-y_0)}{\sinh\frac{1}{2}kD}\right] \tag{24}$$

by

$$\frac{\partial H^*}{\partial y} = kH. \tag{25}$$

The first approximation to the velocity field is then

$$\boldsymbol{v} = \frac{U}{D}\left[y\hat{\mathbf{x}}-2L\sum_{m=1}^{M}A_m\boldsymbol{v}_2^\infty(x,y,2mL;D)\right], \tag{26}$$

in which the along-channel component is given, from (22) and (23), by

$$v_{2x}^\infty = \frac{\partial\psi_2^\infty}{\partial y} = -\frac{1}{2}\ln\left[\frac{\cosh\pi(y-y_0)/L-\cos\pi x/L}{\cosh\pi(y+y_0)/L-\cos\pi x/L}\right]$$

$$-\frac{\pi}{2L}\left[\frac{(y-y_0)\sinh\pi(y-y_0)/L}{\cosh\pi(y-y_0)/L-\cos\pi x/L}-\frac{(y+y_0)\sinh\pi(y+y_0)/L}{\cosh\pi(y+y_0)/L-\cos\pi x/L}\right]$$

$$+\frac{\pi}{L}\sum_{s=1}^{\infty}V_{2x}^\infty\left(\frac{s\pi y}{L},\frac{s\pi y_0}{L};\frac{s\pi D}{L}\right)\cos\frac{s\pi x}{L}-\frac{2\pi y y_0}{DL}, \tag{27}$$

https://doi.org/10.1017/S0022112000002160 Published online by Cambridge University Press

where

$$V_{2x}^{\infty} = -2DH(ky, ky_0; kD) - 2\left(\frac{1}{k} + \frac{\partial}{\partial k}\right)\left[e^{-kD}\frac{\sinh ky \sinh ky_0}{\sinh kD}\right]. \tag{28}$$

The physical interpretation of the coefficients $\{A_m\}$ in (26) is that the force (per unit length) on each cylinder is $8\pi\mu U A_m L/D$. Equations for $\{A_m\}$ can be obtained from (26) by requiring zero mean velocity at each cylinder but the radius $a$ appears only in the term $\ln(2L/\pi a)$ and so the effects of non-zero $\phi$, defined by (21), are essentially ignored. The second approximation constructed below includes potential doublet and Faxén Law terms and takes account of the local shear due to both the imposed flow and the other singularities in order to ensure no slip on each cylinder up to order $a^2/L^2$.

### 2.2. *Higher-order singularities*

The addition of suitable potential doublet terms to (26) yields

$$\boldsymbol{v} = \frac{U}{D}\left[y\hat{\boldsymbol{x}} - 2L\sum_{m=1}^{M} A_m\left\{\boldsymbol{v}_2^{\infty}(x, y, 2mL; D) + \frac{a^2}{4}\left\langle\left(\frac{\partial^2}{\partial x^2} + \frac{\partial^2}{\partial y_0^2}\right)\boldsymbol{v}_2^{\infty}(x, y, y_0; D)\right\rangle_{y_0=2mL}\right\}\right],$$

from which it is noted that the Faxén Law terms are similar and preserve symmetry in $y, y_0$.

Let coefficients $\{G_n\}$ and $\{\mathscr{G}_n\}$ be defined by writing the vector shear rate at $(0, 2nL)$ in the form

$$\frac{U}{2D}\left[(G_n + \mathscr{G}_n)\hat{\boldsymbol{x}} + (-G_n + \mathscr{G}_n)\hat{\boldsymbol{y}}\right].$$

In the velocity field, these coefficients respectively multiply the local rotational and extensional components of the form $(U/2D)[(y - y_0)\hat{\boldsymbol{x}} \mp x\hat{\boldsymbol{y}}]$, which, for no slip at $r = a$ (referred to suitable polar coordinates), respectively require the addition of the stream function terms:

$$-\frac{Ua^2}{2D}\ln r, \qquad \frac{Ua^2}{2D}\left(1 - \frac{a^2}{2r^2}\right)\cos 2\theta.$$

The corresponding additional velocities are, according to (20),

$$\frac{Ua^2}{2D}\left(\hat{\boldsymbol{x}}\frac{\partial}{\partial y} - \hat{\boldsymbol{y}}\frac{\partial}{\partial x}\right)\left\{-\tfrac{1}{2}\ln[x^2 + (y - y_0)^2], \quad \frac{x^2 - (y - y_0)^2}{x^2 + (y - y_0)^2}\left[1 - \frac{\frac{1}{2}a^2}{x^2 + (y - y_0)^2}\right]\right\}$$

$$= -\frac{Ua^2}{2D}\left\{\frac{(y - y_0)\hat{\boldsymbol{x}} - x\hat{\boldsymbol{y}}}{x^2 + (y - y_0)^2}, \quad a^2\frac{(y - y_0)\hat{\boldsymbol{x}} + x\hat{\boldsymbol{y}}}{[x^2 + (y - y_0)^2]^2} + \frac{4x(y - y_0)[x\hat{\boldsymbol{x}} + (y - y_0)\hat{\boldsymbol{y}}]}{[x^2 + (y - y_0)^2]^2}\left[1 - \frac{a^2}{x^2 + (y - y_0)^2}\right]\right\}.$$

The terms with factor $a^4$ are necessary to satisfy no slip at a distance $a$ but are

https://doi.org/10.1017/S0022112000002160 Published online by Cambridge University Press

negligible at distances of order $L$. Moreover, it is possible to write

$$\frac{4x(y-y_0)[x\hat{\boldsymbol{x}}+(y-y_0)\hat{\boldsymbol{y}}]}{[x^2+(y-y_0)^2]^2} = -2\frac{(y-y_0)\hat{\boldsymbol{x}}-x\hat{\boldsymbol{y}}}{x^2+(y-y_0)^2} + 2\frac{\partial}{\partial y_0}\left\{-\hat{\boldsymbol{x}}\tfrac{1}{2}\ln[x^2+(y-y_0)^2]+x\frac{x\hat{\boldsymbol{x}}+(y-y_0)\hat{\boldsymbol{y}}}{x^2+(y-y_0)^2}\right\}, \quad (29)$$

which contains the above rotlet and a stresslet, namely the $y_0$-derivative of the point force singularity already considered.

Thus, in order to complete the construction of $\boldsymbol{v}$ to the required accuracy, it is necessary only to determine the channel flow generated by a row of rotlet singularities. In doing so, the sense of the image rotlets is chosen to be consistent, in terms of the velocity component cancelled at $y = 0$, with the flow generated by the stresslets. This has the effect of both reducing the amount of computation needed for the matrix of coefficients in the equations (35), below, for $\{A_m\}$ and ensuring that the matrix is demonstrably symmetric. The $\hat{\boldsymbol{x}}$ component of the velocity field generated by a periodic array of negatively directed rotlets at $\{(2nL, \pm y_0); -\infty < n < \infty\}$ in the presence of rigid walls at $y = 0, D$ is given by

$$v_{2x}^R = \frac{\pi}{2L}\left[\frac{\sinh[\pi(y-y_0)/L]}{\cosh[\pi(y-y_0)/L]-\cos[\pi x/L]}+\frac{\sinh[\pi(y+y_0)/L]}{\cosh[\pi(y+y_0)/L]-\cos[\pi x/L]} -\frac{2y}{D}+2\sum_{s=1}^{\infty}U_{2x}\left(\frac{s\pi y}{L},\frac{s\pi y_0}{L};\frac{s\pi D}{L}\right)\cos\frac{s\pi x}{L}\right], \quad (30)$$

after imposing a zero pressure gradient and with

$$U_{2x}(ky,ky_0,kD) = -2\mathrm{e}^{-kD}\frac{\sinh ky\cosh ky_0}{\sinh kD} +k\left[\frac{\sinh k(D-y_0)-\sinh ky_0}{\sinh kD-kD}\right]\frac{\partial}{\partial k}\left[\frac{\cosh k(\frac{1}{2}D-y)}{\cosh\frac{1}{2}kD}\right] +k\left[\frac{\sinh k(D-y_0)+\sinh ky_0}{\sinh kD+kD}\right]\frac{\partial}{\partial k}\left[\frac{\sinh k(\frac{1}{2}D-y)}{\sinh\frac{1}{2}kD}\right].$$

By first showing, from (24) and (25), that

$$kDH^* - D\frac{\partial H}{\partial y} = U_{2x}(ky_0,ky,kD)+2\mathrm{e}^{-kD}\frac{\cosh ky\sinh ky_0}{\sinh kD},$$

it is readily observed that

$$2U_{2x}\left(\frac{s\pi y_0}{L},\frac{s\pi y}{L};\frac{s\pi D}{L}\right) = \frac{\partial V_{2x}^{\infty}}{\partial y}\left(\frac{s\pi y}{L},\frac{s\pi y_0}{L};\frac{s\pi D}{L}\right)-\frac{s^2\pi}{L}\psi_s(y,y_0,D), \quad (31)$$

where $\psi_s$ and $V_{2x}^{\infty}$ are respectively given by (23) and (28). The sense of the image rotlets is chosen for consistency with the $y_0$-derivatives of the image point forces, i.e. to produce a zero along-channel velocity at $y = 0$. This furnishes an advantage in the subsequent calculations.

https://doi.org/10.1017/S0022112000002160 Published online by Cambridge University Press

### 2.3. *The $O(\phi)$ approximation*

The shear rates are given, from (26) and (27), by

$$G_n = 1 - 2\pi \sum_{m=1}^{M} E_{nm} A_m, \qquad \mathscr{G}_n = 1 - 2\pi \sum_{m=1}^{M} \mathscr{E}_{nm} A_m, \tag{32}$$

where, after some manipulation,

$$E_{nm} = -\frac{4mL}{D} + \coth \pi(n+m) + 2\sum_{s=1}^{\infty} U_{2x}\left(2\pi ms, 2\pi ns, \frac{s\pi D}{L}\right) - \begin{cases} \coth \pi(n-m) & (n \neq m) \\ 0 & (n = m), \end{cases}$$

$$\tfrac{1}{2}[E_{nm} + \mathscr{E}_{nm}] = -\frac{4mL}{D} + \coth \pi(n+m) - \frac{\pi(n+m)}{2\sinh^2 \pi(n+m)} + \sum_{s=1}^{\infty} \frac{\partial V_{2x}^{\infty}}{\partial y}\left(2\pi ns, 2\pi ms, \frac{s\pi D}{L}\right) - \begin{cases} \coth \pi(n-m) - \dfrac{\pi(n-m)}{2\sinh^2 \pi(n-m)} & (n \neq m) \\ 0 & (n = m), \end{cases} \tag{33}$$

The complete $O(\phi)$ approximation to the velocity field is therefore the following extension of (26):

$$\boldsymbol{v} = \frac{U}{D}\left[y\hat{\boldsymbol{x}} - 2L\sum_{m=1}^{M} A_m \left\{ \boldsymbol{v}_2^{\infty}(x, y, 2mL; D) + \frac{a^2}{4}\left\langle \left(\frac{\partial^2}{\partial x^2} + \frac{\partial^2}{\partial y_0^2}\right) \boldsymbol{v}_2^{\infty}(x, y, y_0; D) \right\rangle_{y_0 = 2mL} \right\} - \frac{a^2}{2}\sum_{q=1}^{M} \left\{ (G_q - 2\mathscr{G}_q)\boldsymbol{v}_2^R(x, y, 2qL; D) + 2\mathscr{G}_q \frac{\partial \boldsymbol{v}_2^{\infty}}{\partial y_0}(x, y, 2qL; D) \right\} \right], \tag{34}$$

after exploiting (29) to construct the last series.

The no-slip condition is approximately imposed by now requiring zero velocity up to $O(\phi)$ at each cylinder centred at $(0, 2nL)$ $\{1 \leqslant n \leqslant M\}$. This involves taking special account of the singularities at this point, including the Faxén Law contribution, substituting (27) and (30) and making use of the coefficients defined by (33) to obtain the following linear system of equations for $\{A_m; 1 \leqslant m \leqslant M\}$:

$$n = A_n \left\{ -\ln \frac{\pi a}{2L} - \frac{1}{2} - \frac{\pi^2 a^2}{12L^2} + \ln \sinh 2\pi n + 2\pi n \coth 2\pi n - \frac{8\pi n^2 L}{D} - \frac{\pi^2 a^2}{4L^2 \sinh^2 2\pi n} + \frac{\pi}{L}\sum_{s=1}^{\infty} V_{2x}^{\infty}\left(2\pi ns, 2\pi ns, \frac{s\pi D}{L}\right) \right.$$

https://doi.org/10.1017/S0022112000002160 Published online by Cambridge University Press

$$+\frac{\pi a^2}{2L}\left[\nabla^2\sum_{s=1}^{\infty}V_{2x}^{\infty}\left(\frac{s\pi y}{L},\frac{s\pi y_0}{L};\frac{s\pi D}{L}\right)\cos\frac{s\pi x}{L}\right]_{(0,2nL,2nL)}\Bigg\}$$

$$+\sum_{m=1,m\neq n}^{M}A_m\Bigg\{-\ln\frac{\sinh\pi|n-m|}{\sinh\pi(n+m)}-\frac{8\pi nmL}{D}-\pi(n-m)\coth\pi(n-m)$$

$$+\pi(n+m)\coth\pi(n+m)+\frac{\pi}{L}\sum_{s=1}^{\infty}V_{2x}^{\infty}\left(2\pi ns,2\pi ms,\frac{s\pi D}{L}\right)$$

$$+\frac{\pi^2a^2}{4L^2\sinh^2\pi(n-m)}-\frac{\pi^2a^2}{4L^2\sinh^2\pi(n+m)}$$

$$+\frac{\pi a^2}{4L}\left[(\nabla^2+\nabla_0^2)\sum_{s=1}^{\infty}V_{2x}^{\infty}\left(\frac{s\pi y}{L},\frac{s\pi y_0}{L};\frac{s\pi D}{L}\right)\cos\frac{s\pi x}{L}\right]_{(0,2nL,2mL)}\Bigg\}$$

$$+\frac{\pi a^2}{8L^2}\sum_{q=1}^{M}[(G_q-2\mathscr{G}_q)E_{qn}+2\mathscr{G}_q(E_{qn}+\mathscr{E}_{qn})]\quad(1\leqslant n\leqslant M),\tag{35}$$

in which the last summation reduces, after substitution of (32) and a cancellation, to

$$\frac{\pi a^2}{8L^2}\sum_{q=1}^{M}(E_{qn}+2\mathscr{E}_{qn})-\frac{\pi^2a^2}{4L^2}\sum_{m=1}^{M}A_m\sum_{q=1}^{M}(E_{qm}E_{qn}+2\mathscr{E}_{qm}\mathscr{E}_{qn}).$$

This last identity establishes the symmetry of the matrix of coefficients in (35), whose evaluation is assisted by (28), (31) and (33).

### 2.4. *Mean flow along the channel*

In regions unobstructed by cylinders, i.e.$|y-2nL|\geqslant a$ $(1\leqslant n\leqslant M)$, the mean value of $\boldsymbol{v}$ is, from (34)

$$\frac{U}{D}\hat{\boldsymbol{x}}\left[y-4\pi\sum_{m=1}^{M}A_m\left(\min(y,2mL)-2mL\frac{y}{D}\right)\right.$$

$$\left.+\frac{\pi a^2}{2L}\sum_{q=1}^{M}(G_q+2\mathscr{G}_q)\left(H(y-2qL)-\frac{y}{D}\right)\right].$$

These piecewise linear profiles are smoothly connected via regions in which the cylinders reduce the volume. The above analysis enables it to be shown, for terms up to order $a$, that this is achieved by the mean flow

$$\frac{U}{D}\left(1-\frac{\sqrt{a^2-d^2}}{L}\right)\hat{\boldsymbol{x}}\left[(2nL+d)-8\pi L\left(1-\frac{2nL+d}{D}\right)\sum_{m=n}^{M}mA_m\right.$$

$$\left.-4\pi(2nL+d)\sum_{m=1}^{n-1}A_m\left(1-\frac{2ML}{D}\right)-4A_n[d\arccos(d/a)-\sqrt{a^2-d^2}]\right],$$

where $y=2nL+d$ $(1\leqslant n\leqslant M)$ and $|d|<a$.

https://doi.org/10.1017/S0022112000002160 Published online by Cambridge University Press

In particular, the mean value of $\boldsymbol{v}$ for $2ML + a < y < D$ is

$$\frac{U}{D}\hat{\boldsymbol{x}}\left[y - 8\pi L\left(1 - \frac{y}{D}\right)\sum_{m=1}^{M} mA_m - \frac{\pi a^2}{2L}\left(1 - \frac{y}{D}\right)\sum_{q=1}^{M}(G_q + 2\mathscr{G}_q)\right],$$

from which the quantity $f_1/f_2$ in (6) is readily determined. Moreover, the constant shear in the open channel allows $f_2$, defined by (5), to be set equal to unity.

### 2.5. *Modifications for an equilateral array*

Suppose that the centres of the cylinders are instead placed at $\{(m+2l)L, \sqrt{3}mL; 1 \leqslant m \leqslant M, -\infty < l < \infty\}$. Then, corresponding to (34),

$$\begin{aligned}\boldsymbol{v} = \frac{U}{D}\Bigg[&y\hat{\boldsymbol{x}} - \sqrt{3}L\sum_{m=1}^{M} A_m\Bigg\{\boldsymbol{v}_2^{\infty}(x - mL, y, \sqrt{3}mL; D)\\ &+\frac{a^2}{4}\left\langle\left(\frac{\partial^2}{\partial x^2} + \frac{\partial^2}{\partial y_0^2}\right)\boldsymbol{v}_2^{\infty}(x, y, y_0; D)\right\rangle_{y_0=\sqrt{3}mL}\Bigg\}\\ &-\frac{a^2}{2}\sum_{q=1}^{M}\left\{(G_q - 2\mathscr{G}_q)\boldsymbol{v}_2^{R}(x - qL, y, \sqrt{3}qL; D) + 2\mathscr{G}_q\frac{\partial \boldsymbol{v}_2^{\infty}}{\partial y_0}(x - qL, y, \sqrt{3}qL; D)\right\}\Bigg],\end{aligned} \tag{36}$$

in which equations (32) are modified to

$$G_n = 1 - \sqrt{3}\pi\sum_{m=1}^{M} E_{nm}A_m, \qquad \mathscr{G}_n = 1 - \sqrt{3}\pi\sum_{m=1}^{M}\mathscr{E}_{nm}A_m \tag{37}$$

and the coefficient matrices are now given, instead of (33), by

$$\begin{aligned}E_{nm} = &-\frac{2\sqrt{3}mL}{D} + \frac{\sinh\pi\sqrt{3}(n+m)}{\cosh\pi\sqrt{3}(n+m) - (-1)^{n-m}}\\ &+2\sum_{s=1}^{\infty} U_{2x}\left(\sqrt{3}\pi ms, \sqrt{3}\pi ns, \frac{s\pi D}{L}\right)(-1)^{(n-m)s}\\ &-\begin{cases}\dfrac{\sinh\pi\sqrt{3}(n-m)}{\cosh\pi\sqrt{3}(n-m) - (-1)^{n-m}} & (n \neq m)\\ 0 & (n = m),\end{cases}\end{aligned}$$

$$\begin{aligned}\tfrac{1}{2}[E_{nm} + \mathscr{E}_{nm}] = &-\frac{2\sqrt{3}mL}{D} + \frac{\sinh\sqrt{3}\pi(n+m) - \pi\sqrt{3}(n+m)(-1)^{n-m}}{\cosh\pi\sqrt{3}(n+m) - (-1)^{n-m}}\\ &+\sum_{s=1}^{\infty}\frac{\partial V_{2x}^{\infty}}{\partial y}\left(\sqrt{3}\pi ns, \sqrt{3}\pi ms, \frac{s\pi D}{L}\right)(-1)^{(n-m)s}\end{aligned}$$

https://doi.org/10.1017/S0022112000002160 Published online by Cambridge University Press

$$-\begin{cases} \dfrac{\sinh\sqrt{3}\pi(n-m)-\pi\sqrt{3}(n-m)(-1)}{\cosh\pi\sqrt{3}(n-m)-(-1)^{n-m}} & (n\neq m) \\ 0 & (n=m). \end{cases} \tag{38}$$

Thus the simultaneous equations (35) are modifed to

$$\begin{aligned} n = A_n\Bigg\{ & -\ln\frac{\pi a}{2L}-\frac{1}{2}-\frac{\pi^2a^2}{12L^2}+\ln\sinh\sqrt{3}\pi n+\sqrt{3}\pi n\coth\sqrt{3}\pi n \\ & -\frac{6\pi n^2L}{D}-\frac{\pi^2a^2}{4L^2\sinh^2\sqrt{3}\pi n}+\frac{\pi}{L}\sum_{s=1}^{\infty}V_{2x}^{\infty}\left(\sqrt{3}\pi ns,\sqrt{3}\pi ns,\frac{s\pi D}{L}\right) \\ & +\frac{\pi a^2}{2L}\left[\nabla^2\sum_{s=1}^{\infty}V_{2x}^{\infty}\left(\frac{s\pi y}{L},\frac{s\pi y_0}{L};\frac{s\pi D}{L}\right)\cos\frac{s\pi x}{L}\right]_{(0,\sqrt{3}nL,\sqrt{3}nL)}\Bigg\} \\ & +\sum_{m=1,m\neq n}^{M}A_m\Bigg\{-\frac{1}{2}\ln\left[\frac{\cosh\pi\sqrt{3}(n-m)-(-1)^{n-m}}{\cosh\pi\sqrt{3}(n+m)-(-1)^{n-m}}\right]-\frac{6\pi nmL}{D} \\ & -\frac{\pi\sqrt{3}}{2}\left[\frac{(n-m)\sinh\pi\sqrt{3}(n-m)}{\cosh\pi\sqrt{3}(n-m)-(-1)^{n-m}}-\frac{(n+m)\sinh\pi\sqrt{3}(n+m)}{\cosh\pi\sqrt{3}(n+m)-(-1)^{n-m}}\right] \\ & +\frac{\pi}{L}\sum_{s=1}^{\infty}V_{2x}^{\infty}\left(\sqrt{3}\pi ns,\sqrt{3}\pi ms,\frac{s\pi D}{L}\right) \\ & +\frac{\pi^2a^2}{2L^2}\left[\frac{1}{\cosh\pi\sqrt{3}(n-m)-(-1)^{n-m}}-\frac{1}{\cosh\pi\sqrt{3}(n+m)-(-1)^{n-m}}\right] \\ & +\frac{\pi a^2}{4L}\left[(\nabla^2+\nabla_0^2)\sum_{s=1}^{\infty}V_{2x}^{\infty}\left(\frac{s\pi y}{L},\frac{s\pi y_0}{L};\frac{s\pi D}{L}\right)\cos\frac{s\pi x}{L}\right]_{(0,\sqrt{3}nL,\sqrt{3}mL)}\Bigg\} \\ & +\frac{\pi a^2}{4\sqrt{3}L^2}\sum_{q=1}^{M}[(G_q-2\mathscr{G}_q)E_{qn}+2\mathscr{G}_q(E_{qn}+\mathscr{E}_{qn})] \quad (1\leqslant n\leqslant M), \end{aligned} \tag{39}$$

in which the last summation reduces, after substitution of (32) and a cancelation, to

$$\frac{\pi a^2}{4\sqrt{3}L^2}\sum_{q=1}^{M}(E_{qn}+2\mathscr{E}_{qn})-\frac{\pi^2a^2}{4L^2}\sum_{m=1}^{M}A_m\sum_{q=1}^{M}(E_{qm}E_{qn}+2\mathscr{E}_{qm}\mathscr{E}_{qn}).$$

The mean value of $\boldsymbol{v}$ for $\sqrt{3}ML+a<y<D$ is now

$$\frac{U}{D}\hat{\boldsymbol{x}}\left[y-6\pi L\left(1-\frac{y}{D}\right)\sum_{m=1}^{M}mA_m-\frac{\pi a^2}{2L}\left(1-\frac{y}{D}\right)\sum_{q=1}^{M}(G_q+2\mathscr{G}_q)\right]$$

and the relation to (5) and (6) is unchanged.

https://doi.org/10.1017/S0022112000002160 Published online by Cambridge University Press

### 2.6. *Modifications for pressure-driven flow*

Suppose that the basic shear flow $U(y/D)\hat{\boldsymbol{x}}$ is replaced by

$$\frac{G}{2\mu}y(D-y)\hat{\boldsymbol{x}} \qquad \left(G=\frac{\Delta P}{2L}\right),$$

where $G$ denotes, as in (7), the mean pressure gradient in the $-\hat{\boldsymbol{x}}$-direction. Then, corresponding to (34),

$$\boldsymbol{v}=\frac{GD}{2\mu}\left[y\left(1-\frac{y}{D}\right)\hat{\boldsymbol{x}}-2L\sum_{m=1}^{M}A_m\left\{\boldsymbol{v}_2^{\infty}(x,y,2mL;D)\right.\right.$$
$$\left.+\frac{a^2}{4}\left\langle\left(\frac{\partial^2}{\partial x^2}+\frac{\partial^2}{\partial y_0^2}\right)\boldsymbol{v}_2^{\infty}(x,y,y_0;D)\right\rangle_{y_0=2mL}\right\}$$
$$\left.-\frac{a^2}{2}\sum_{q=1}^{M}\left\{(G_q-2\mathscr{G}_q)\boldsymbol{v}_2^{R}(x,y,2qL;D)+2\mathscr{G}_q\frac{\partial\boldsymbol{v}_2^{\infty}}{\partial y_0}(x,y,2qL;D)\right\}\right], \tag{40}$$

in which equations (32) are modified to

$$G_n=1-\frac{4nL}{D}-2\pi\sum_{m=1}^{M}E_{nm}A_m, \qquad \mathscr{G}_n=1-\frac{4nL}{D}-2\pi\sum_{m=1}^{M}\mathscr{E}_{nm}A_m \tag{41}$$

and the coefficient matrices are still given by (33). Thus, on the left-hand side of the simultaneous equations (35), $n$ is replaced by

$$n\left(1-\frac{2nL}{D}\right)-\frac{a^2}{4DL}$$

and

$$-\frac{\pi a^2}{8L^2}\sum_{q=1}^{M}(E_{qn}+2\mathscr{E}_{qn}) \text{ by } -\frac{\pi a^2}{8L^2}\sum_{q=1}^{M}\left(1-\frac{4qL}{D}\right)(E_{qn}+2\mathscr{E}_{qn}).$$

The mean value of $\boldsymbol{v}$ for $2ML+a<y<D$ is

$$\frac{GD}{2\mu}\hat{\boldsymbol{x}}\left(1-\frac{y}{D}\right)\left[y-8\pi L\sum_{m=1}^{M}mA_m-\frac{\pi a^2}{2L}\sum_{q=1}^{M}(G_q+2\mathscr{G}_q)\right]$$

in which the shear rate now varies linearly with $y$. Since the slip velocity is small, this expression furnishes an interfacial shear rate $\dot{\gamma}_w\simeq GW/2\mu$, consistent with (9).

## 3. Results

### 3.1. *Comparisons to established results*

Now that solutions are available for the velocity fields, the first obligation is to provide evidence that the solutions are correct and that calculations based on them are carried out correctly. Unfortunately there are no special cases of rods in channels which facilitate a direct comparison to a known result. The only known solutions for arrays of rods are those for unbounded arrays, i.e. those without edges. Such an array can be simulated using the present technique by completely filling the channel with small rods so that flow through the core is essentially flow through an unbounded

https://doi.org/10.1017/S0022112000002160 Published online by Cambridge University Press

| | | $k/a^2$, Present results | | | | |
|---|---|---|---|---|---|---|
| | | $M$ | 9 | 19 | 5 | 5 |
| | $k/a^2$ | $D/L$ | 20 | 40 | 20 | 40 |
| $\phi$ | Formula (42) | $2ML/D$ | 0.9 | 0.95 | 1/2 | 1/4 |
| 0.002 | 296 | | | | 298 | 302 |
| 0.004 | 126 | | | | 127 | 131 |
| 0.006 | 76.1 | | | | 76.2 | 76.5 |
| 0.010 | 39.4 | | 39.4 | 39.4 | 39.4 | 39.4 |
| 0.020 | 15.5 | | 15.5 | 15.5 | 15.5 | 15.5 |
| 0.040 | 5.70 | | 5.69 | 5.70 | 5.69 | 5.70 |
| 0.060 | 3.04 | | 3.04 | 3.04 | 3.04 | 3.04 |
| 0.100 | 1.283 | | 1.28 | 1.28 | 1.28 | 1.28 |

TABLE 1. Comparison of $k/a^2$ values.

array. Hence calculations were carried out with the channel completely filled with nine, and then 19, equally-spaced rows of rods for an applied pressure gradient. The velocity distributions between adjacent rows were found to be identical, and the common distribution was averaged to yield the drift velocity $U_D$. From $U_D$, the permeability $k$ was found from Darcy's law. Values of $k$ over a range in $\phi$ were compared to values of $k$ calculated from the established formula for a square array, for which there is agreement from several sources on the first three terms (Jackson & James 1986):

$$\frac{k}{a^2} = \frac{1}{8\phi}\left[\ln\frac{1}{\phi} - 1.476 + 2\phi + O(\phi^2)\right]. \tag{42}$$

As a further check, values of $k$ were calculated for rods only partially filling the channel, because flow through the central portion of the array still approximates flow through an unbounded array. These calculations were carried out for quarter- and half-filled channels, with various numbers of rows. Starting from the second row, the averaged velocity was found to be the same from row to row, even for as few as five rows. The average velocity was again used to find the array permeability. All of the results for $k$ are presented in table 1, for $\phi$ ranging from 0.002 to 0.1. The second column gives values of $k/a^2$ from the formula above, the next two columns are values for completely-filled channels, and the last two are values for partially-filled channels.

The table shows excellent agreement between values from the present work and values from the established formula, (42). In fact, agreement is generally to three significant figures, which is better than expected because the order of the neglected terms in the analyses is $o(\phi)$. For the partially-filled channels, calculations were carried out for various numbers of rows, but only results for the 5-row cases are presented. In these cases, $k$ was based on the average velocity between the 2nd and 3rd rows (the same as that between the 3rd and 4th rows) and these $k$ values agree well with those for completely-filled channels. The close agreement also implies that shear effects occur only between the wall and the 1st row and between the 4th row and the interface. Shear does not seem to persist from one row to the next. But the crucial point is that the table confirms that the present technique is accurate.

https://doi.org/10.1017/S0022112000002160 Published online by Cambridge University Press

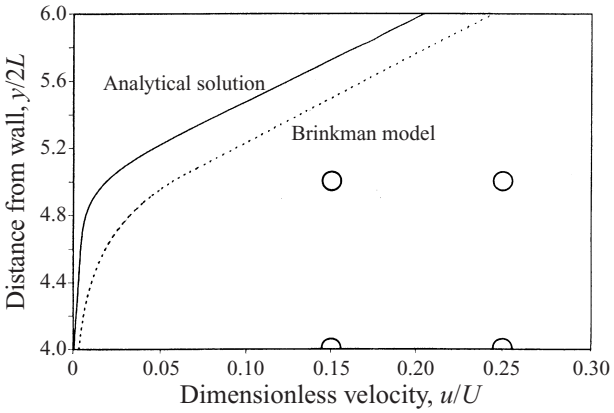



FIGURE 4. Dimensionless velocity profiles close to the interface of a square array. The array consists of five rows of cylinders occupying the lower 1/2 of the channel, and shear flow is created by the unseen upper wall moving at speed $U$ (at ordinate value 10). The four cylinders shown are in the top two rows of the array; they are drawn to scale and located relative to the velocity profiles. The solid upper curve is the profile found by the present technique, evaluated at the midplane between cylinders, and the dashed curve is the profile predicted by Brinkman's equation in the porous medium and Stokes equation in the channel. $\phi = 0.01$, $M = 5$, $D/L = 20$, $2ML/D = 1/2$.

### 3.2. *Shear-driven flows*

When the flow is shear-driven, the flow changes from shear flow in the channel to zero flow in the array, and figure 4 illustrates how quickly the change takes place. The physical situation in the figure is an array of five rows occupying the bottom half of the channel. The figure focuses on the interfacial region, starting at the 4th row, and the rods shown are to scale. The upper curve is a velocity profile predicted by the present work and the lower curve, the 'Brinkman Model', is obtained by setting the pressure gradient equal to zero in the Stokes and Brinkman equations and matching the linear velocity distribution in the channel, where the velocity gradient is $\dot{\gamma}$, with the exponential velocity distribution in the porous medium, as given by the solution of the Brinkman equation in (17). The two profiles in figure 4 actually converge at the outer wall where the ordinate is 10 and abscissa is 1.0, but this convergence is well outside the plot. Comparing these two profiles is not strictly valid because the analytical profile is the profile along the midplane between the rods; hence it is a particular profile and not an average like the Brinkman profile. However, if the analytical profile were the average (in the $x$-direction), the difference between the profiles would be even larger. The midplane profile is shown instead because it illustrates the maximum penetration of the outer flow and because the average profile turns out to consist of straight segments connected by curves, as described in § 2.4, and so is less useful. What figure 4 makes especially clear is that, for widely spaced rods, there is much less penetration than suggested by intuition and predicted by Brinkman's equation.

Attention is now focused on the slip velocity $U_s$, the quantity of primary interest. In this work, the slip velocity is the average velocity on the plane tangent to the outer edges of the cylinders in the first row. In our view, this plane represents the interface better than any other simply-located plane, including the plane through the cylinder axes, which has been favoured by some authors (e.g. Larson & Higdon 1986). The tangent plane is the most logical one for flow in the channel because it is the first contact of that flow with the array, thus becoming a boundary of the channel. In

https://doi.org/10.1017/S0022112000002160 Published online by Cambridge University Press

| Number of rows | Spacing | Filling fraction | $U_s/\dot{\gamma}\sqrt{k}$ $\phi$ | | | |
|---|---|---|---|---|---|---|
| $M$ | $D/L$ | $2ML/D$ | 0.0001 | 0.001 | 0.01 | 0.10 |
| 5 | 40 | 1/4 | 0.352 | 0.294 | 0.248 | 0.234 |
| 10 | 80 | 1/4 | 0.352 | 0.294 | 0.247 | 0.231 |
| 20 | 160 | 1/4 | 0.352 | 0.294 | 0.247 | 0.230 |
| 5 | 20 | 1/2 | 0.352 | 0.294 | 0.250 | 0.239 |
| 20 | 80 | 1/2 | 0.352 | 0.294 | 0.250 | 0.231 |
| 15 | 40 | 3/4 | 0.352 | 0.294 | 0.248 | 0.231 |

TABLE 2. Values of the dimensionless slip velocity, $U_s/\dot{\gamma}\sqrt{k}$, for square arrays of rods, partially filling the channel. Note: for the Brinkman model, $U_s/\dot{\gamma}\sqrt{k} = 1.0$, from equation (17).

showing how $U_s$ depends on flow and array conditions, $U_s$ will be related to the external shear rate, following the dimensional reasoning at the outset, and not to the wall velocity as in figure 4. As follows from equations (2) and (3), $U_s$ will be presented in terms of the dimensionless group $U_s/\dot{\gamma}\sqrt{k}$. This group is the inverse of the slip coefficient $\alpha$ introduced earlier and used in previous studies. We prefer to use a dimensionless group which is proportional to $U_s$ because $U_s$ is the quantity of interest. $U_s/\dot{\gamma}\sqrt{k}$ is obviously a dimensionless slip velocity but the group can equally be considered a dimensionless length because $U_s/\dot{\gamma}$ is a measure of the depth of penetration and $\sqrt{k}$ is the length scale for the porous medium. Here the emphasis is on slip rather than penetration; accordingly $U_s/\dot{\gamma}\sqrt{k}$ will be referred to hereafter as the dimensionless slip velocity.

Values of $U_s/\dot{\gamma}\sqrt{k}$ were calculated for square arrays over an extensive range of conditions: for various numbers of rows, for a three-decade range in $\phi$, and for different filling fractions (the fraction of the channel occupied by the porous medium). These values are presented in table 2. To put these values in context, it is noted that the value of $U_s/\dot{\gamma}\sqrt{k}$ is 1 when the Brinkman model is used, which comes from matching equation (17) with the linear velocity distribution $U_s + \dot{\gamma}\tilde{y}$ in the channel.

The first three rows of the table pertain to channels 1/4-filled with arrays. The entries show that, as $M$ increases from 5 to 20 with $\phi$ fixed, $U_s/\dot{\gamma}\sqrt{k}$ changes only in the third significant figure. That is, the result is independent of the size of the cylinders, relative to the width of the channel. The last three rows, for 1/2-filled and 3/4-filled channels, give the same values of $U_s/\dot{\gamma}\sqrt{k}$ as those for the 1/4-filled channels, for the same values of $\phi$. Table 2 therefore demonstrates that the dimensionless slip velocity for a square array depends only on one parameter, the solid volume fraction.

Because equation (3) states that $U_s/\dot{\gamma}\sqrt{k}$ should not depend on $\phi$, the actual dependence has been plotted and is the dashed curve in figures 7 to 9 below. The curve demonstrates that the dependence is not strong and shows more clearly than table 2 that $U_s/\dot{\gamma}\sqrt{k}$ is virtually constant at 0.25 over the $\phi$ range from 0.01 to 0.1. A constant value in this range is useful because the most practical range in $\phi$ is that decade.

In the dimensional reasoning which led to equation (3), it was assumed that the length scale of the porous medium is given by a single parameter, $\sqrt{k}$. With a rod

https://doi.org/10.1017/S0022112000002160 Published online by Cambridge University Press

array, however, there are two length scales, and so (3) and the other general relations in the dimensional reasoning need to be modified accordingly. When two length scales are used instead of one, it is straightforwardly found that $U_s/\dot{\gamma}\sqrt{k}$ then depends on $\phi$, for a square array. Hence table 2 and the dashed curve are consistent with the dimensionless equations when they are revised. At the same time, the dependence on $\phi$ is peculiar because one might expect that, if $U_s/\dot{\gamma}\sqrt{k}$ were constant or approximately so over a range in $\phi$, the range would be the asymptotic one, with $\phi$ going to zero. It is a mystery to us why $U_s/\dot{\gamma}\sqrt{k}$ is constant over the $\phi$ decade from 0.008 to 0.08.

The value of unity for $U_s/\dot{\gamma}\sqrt{k}$ from the Brinkman model, as described in the text and as noted at the bottom of table 2, is much higher than the values in the table. This comparison shows that the Brinkman model overpredicts the slip velocity by a factor of about four, and this outcome is consistent with the curves in figure 4. This overprediction would not be reduced much if the effective viscosity $\mu^*$ were reintroduced and made larger than $\mu$. As described in the Introduction, prior work has established that $\mu^*/\mu$ exceeds unity by $O(\phi)$. But an $O(\phi)$ modification will not cause the Brinkman equation to fit much better nor will it correct the four-fold discrepancy at the interface. Furthermore, table 2 shows that the discrepancy is not a function of $\phi$. Hence even if the Brinkman equation were to include $\mu^*$, it would still overpredict the slip velocity by several times.

The above results apply to square arrays, and corresponding calculations were carried out for triangular arrays of the type illustrated in figure 3. A comparison between the two geometries is presented in table 3.

In the table, there are only small differences between the two geometries, differences which may not be significant because they are of the same order as the neglected terms in the analysis. At the same time, only small differences would be expected because of minimal penetration, as shown in figure 4. That is, the geometrical difference in the two arrays starts in the second row and figure 4 reveals that the outer flow barely penetrates to the second row. Hence this geometrical variation does not produce a different result. Other geometrical variations with rods were not explored because calculations using the present technique are too difficult.

### 3.3. *Pressure-driven flows*

Velocity distributions were calculated for flows driven by pressure, for the same array configurations as those for the shear-driven flows. A sample result is shown in figure 5. The solid volume fraction of the array in the figure is very small and was chosen to produce a visible slip velocity. Two velocity profiles are presented, one predicted for the midplane by the present method and the other predicted using Stokes and Brinkman's equations. In these equations, the pressure gradient term is not zero but is constant, and the prediction based on the two equations is obtained by matching the quadratic profile in the channel (the solution of Stokes equation) with the solution of Brinkman's equation in the array. The matching consists of making the velocity and the velocity gradient (or the shear stress) continuous across the interface. The velocity profile found from Brinkman's equation contains the uniform drift velocity $U_D$ as well as the usual exponential term. Both profiles in figure 5 show the expected parabolic shape in the channel and the near-uniform velocity in the array. The only place where the two profiles differ significantly is at the interface, which again shows that the Brinkman equation significantly overpredicts the slip velocity.

Figure 5 confirms that a low value of $\phi$ is indeed required for a significant slip velocity, at least relative to the velocity in the channel. Our calculations revealed that the velocity depends on the fraction of the channel filled by the porous medium.

https://doi.org/10.1017/S0022112000002160 Published online by Cambridge University Press

| | $U_s/\dot{\gamma}\sqrt{k}$ | | | | |
|---|---|---|---|---|---|
| $\phi$ | 0.001 | 0.003 | 0.01 | 0.03 | 0.10 |
| Square | 0.294 | 0.269 | 0.250 | 0.248 | 0.236 |
| Triangular | 0.298 | 0.275 | 0.256 | 0.255 | 0.255 |

TABLE 3. Square versus triangular arrays.

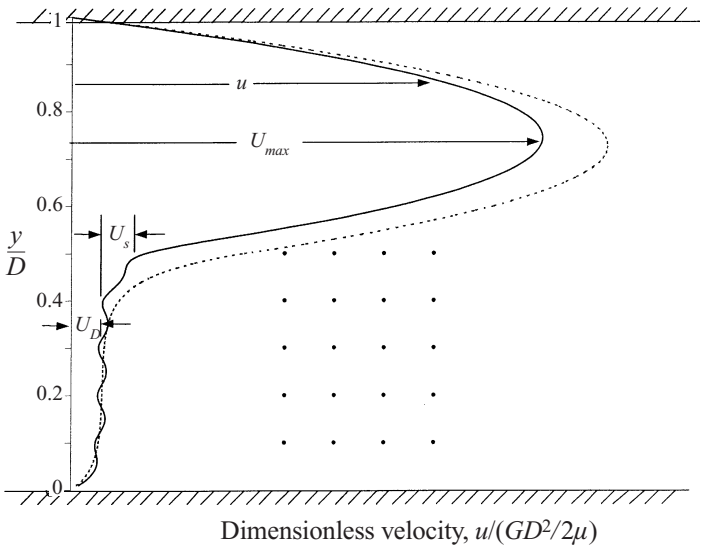



FIGURE 5. Velocity distributions for pressure-driven flow in a channel half filled with a square array of widely-separated cylinders. As in figure 4, the solid curve is the profile found by the present technique and the dashed curve is the profile predicted by Brinkman's equation in the porous medium and Stokes equation in the channel. $M = 5$, $D/L = 20$, $2ML/D = 1/2$, $\phi = 0.001$.

To show how $U_s$ depends on $\phi$ and the filling fraction, figure 6 presents values of $U_s/U_m$ over ranges in both parameters, where $U_m$ is the velocity in the middle of the channel and approximates the maximum velocity. The figure shows that $U_s/U_m$ decreases gradually over three decades in $\phi$, and that $U_s/U_m$ is less than 10% for filling fractions up to 1/2. $U_s/U_m$ rises above 10% only when $\phi$ is less than about 0.003 and when the channel space is limited, as when the filling fraction is 3/4. Perhaps the most important result in the graph is that, in the practical range of $\phi$, i.e. for $\phi$ above 0.01, the slip velocity is from 1% to 10% of the maximum velocity, which means that slip can be ignored in many engineering situations.

The results from both types of flow demonstrate that penetration is small, even for widely separated cylinders. This finding suggests that the outside row provides a far larger resistance than the other rows, and this aspect is being explored in further work.

### 3.4. *Comparison of shear-driven and pressure-driven flows*

In the dimensional reasoning presented at the beginning, it was argued that shear-driven and wall-driven cases are related because the velocity distribution near the wall in pressure-driven flow is approximately linear and thus is similar to the linear profile

https://doi.org/10.1017/S0022112000002160 Published online by Cambridge University Press

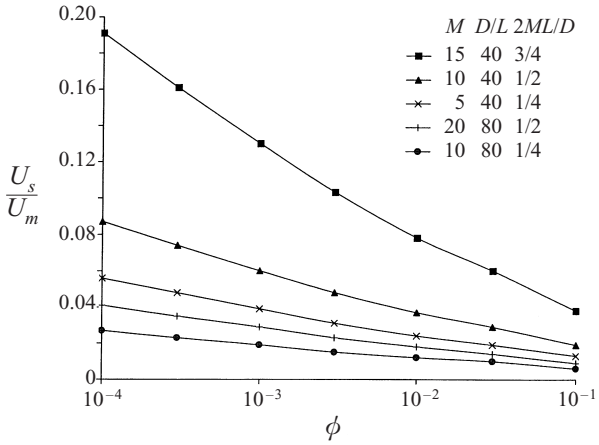



FIGURE 6. The slip velocity, relative to the mid-channel velocity $U_m$, for pressure-driven flow over and through a square array of cylinders. The slip velocity decreases with $\phi$, as expected, and depends on the number of rows ($M$) and on the width of the array relative to the total width of the channel ($2ML/D$).

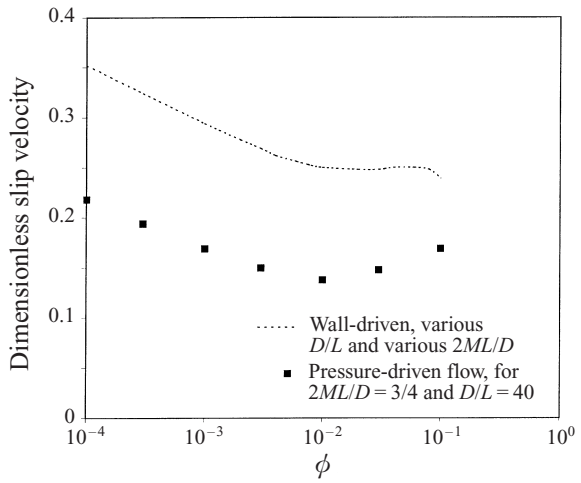



FIGURE 7. Comparison of the dimensionless slip velocity for shear- and pressure-driven flows. The dashed curve pertains to shear-driven flow for all array conditions (table 2). The data points pertain to pressure-driven flow through a square array of 15 cylinders occupying 3/4 of the channel width.

in shear-driven flow. More specifically, equation (13) shows that, when the interface is far from the channel wall in a pressure-driven flow, the slip velocity should be the same as that in the comparable shear-driven case. Data from the two flows are presented in figures 7 to 9. Data for the 3/4-filled channel are presented first because the outer wall is closest and its proximity makes the two flow types least similar. In figure 7, the dashed line is the dimensionless slip velocity for shear-driven flows – the line pertains to all filling fractions, as shown by table 2 – and the data points are for pressure-driven flows. The data in figure 7 are for 15 rows of rods in the channel with $D/L$ set equal to 40, and so the distance to the wall $W$ is five times the distance between rods, $2L$. Since $W/2L$ is not large, it is expected that the wall influences the flow at the interface. The figure shows that the influence is large, because the slip

https://doi.org/10.1017/S0022112000002160 Published online by Cambridge University Press

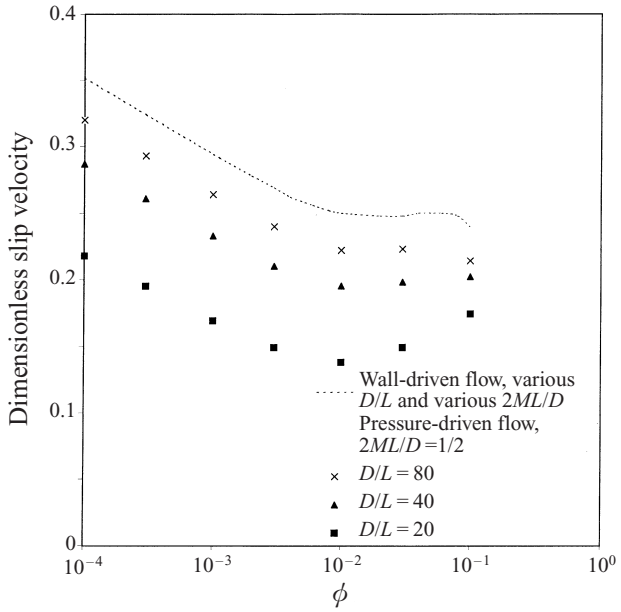



FIGURE 8. As figure 7 but when the cylinder array occupies half of the channel. The data points are for pressure-driven flow for various combinations of cylinder sizes and numbers of rows that create a 1/2-filled channel.

velocity is 40% less than that in the equivalent shear-driven flow. In this case, then, the wall retards the flow at the interface significantly.

The wall should have less influence when it is further away, and figure 8 presents data for 1/2-filled channels. The data sets in figure 8, for different values of $D/L$, correspond to different values of the ratio $W/2L$. For the data set $D/L = 20$, $W/2L$ is 5 and so the data should be identical to the values in the previous graph, as indeed they are. For the intermediate data set, $W/2L$ is 10 and for the highest, $W/2L$ is 20. At 20, the outer wall should have little influence but it still causes the slip velocity to be about 10% lower than that for the equivalent shear-driven case.

When the channel is 1/4-filled, differences between the two cases should be even smaller and data are given in figure 9. For the three values of $D/L$ in the plot, the corresponding values of $W/2L$ are 15, 30 and 60. Only in the last case are slip velocities within several percent of the shear-driven values. Hence this last plot demonstrates that $W/2L$ must be of order $10^2$ for the two cases to coincide.

### 3.5. *Comparisons to prior studies*

In relating the present results to prior ones, the previous study which is most relevant is the numerical study by Larson & Higdon (1987) because their study pertains to shear-driven flow over a square array of rods. As described earlier in this paper, they found circulation between the two outermost rows for $\phi$ between about 0.04 and 0.1. We did not find any circulation for $\phi$ between 0.001 and 0.1 – only positive values of the velocity in the shear direction. However, velocities inside the medium are a small fraction of the wall velocity (figure 4) and the $O(\phi)$ accuracy of the present technique may not be adequate for the small velocities associated with circulation. Including more terms in the present technique would not only be prohibitively difficult but also

https://doi.org/10.1017/S0022112000002160 Published online by Cambridge University Press

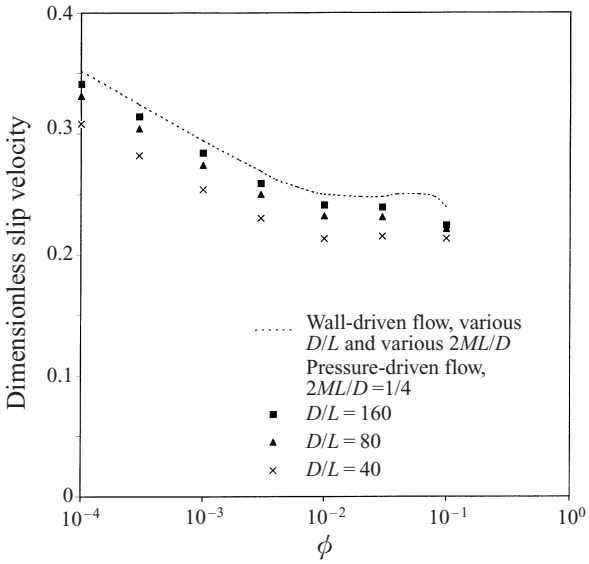



FIGURE 9. As figure 7 but for square arrays filling 1/4 of the channel. The data pertain to different combinations of row numbers and cylinder sizes that make the channel 1/4-filled.

may not provide the desired accuracy because almost equal terms in the array cancel. Hence it seems that circulation must be investigated numerically or experimentally.

Larson & Higdon found values of $U_s$ but direct comparisons between our values and theirs are difficult because they calculated $U_s$ by two methods and the two yielded widely-different values, as described in the introductory section of this paper. By either method, they found mostly negative values for $U_s$, while we found only positive values. The only possible type of comparison is to an order of magnitude for their positive values of $U_s$, which are for highly dilute systems. When their dimensionless velocity is re-cast in terms of our dimensionless slip velocity and when allowance is made for their choice of interface (theirs is the plane through cylinder centres), their values of our dimensionless slip velocity lie between 0 to 0.4, which bracket our near-constant value of 0.3 in the dilute regime.

In the other theoretical work involving an array of rods (Sahraoui & Kaviany 1992), the $\phi$ range was 0.2 and above. When their results are expressed in terms of our dimensionless slip velocity, this quantity is 0.25 at $\phi = 0.2$ and increases with $\phi$. Our $\phi$ range is up to 0.1 and so does not overlap with theirs. However, we found the dimensionless velocity to be constant at 0.25 for $\phi$ up to 0.1, as presented in table 2, and so the two sets of results are compatible.

The present findings should be related to the work of Sangani & Behl (1988) because the large discrepancies we found with Brinkman's equation appear to be inconsistent with their findings. Their porous media consisted of regularly-spaced spheres and, with $\mu^*$ set equal to $\mu$ in Brinkman's equation, they found that the "agreement between the exact numerical calculations and the Brinkman equation is generally very good" for the slip velocity. But they defined the slip velocity on a different plane than we did, one beyond the tangent plane for $\phi$ less than 0.1. Their further distance is $L - a$ in our notation. Further into the external flow, velocities are much higher of course, and so better agreement would be expected. We would have obtained good agreement too had we selected a plane further out. In our case,

https://doi.org/10.1017/S0022112000002160 Published online by Cambridge University Press

because $U_s/\hat{\gamma}\sqrt{k}$ is close to 0.3 over a wide range in $\phi$, the further distance is about $0.7\sqrt{k}$. This distance is not $L-a$ but it is of the same order and the difference is most likely related to the different geometries – a cubical array of spheres versus a square array of rods.

The present work can also be related to work on flow penetration into a polymer brush. Doyle, Shaqfeh & Gast (1998) used Brownian dynamics simulations to determine the chain density and velocity field within a brush over which there is a shear flow. Their results show that the density in the outer region of the brush is about 1/10 the density in the interior and that the shear flow penetrates about the first 20% of the brush, i.e. it penetrates the region of low density. These values are evident in their figure 2(*a*), which also shows that the velocity $U_s$ is about $0.6U$, where $U$ is the velocity of the outer wall. This value of $U_s$ can be related to present values when the variable chain density and the closer outer wall are accounted for. As to density, since the overall $\phi$ value (or areal fraction in their terms) is 0.125 in the brush of figure 2(*a*), the $\phi$ value in the outer region is about 0.012. This value is close to 0.01 in our figure 4, where it is seen that $U_s$ is about $0.025U$. But the open channel in figure 4 is much wider than the one in Doyle *et al.* (1998), specifically 1/0.13 wider. If our open section had this width, then our value of $U_s$ would be about $0.025U/0.13$ or about $0.2U$, which is of the same order as their value of $0.6U$. Better agreement should not be expected because the two situations – flexible chains extending into the flow versus rods across the flow in a fixed array – are only roughly comparable. Even so, a higher $U_s$ would be expected for the brush because the flow can penetrate this arrangement more easily.

Comparisons can also be made to experimental values. As noted in the Introduction, experimental investigators determined values of $\alpha$, the inverse of our dimensionless slip velocity. For a variety of materials, the experimenters found values of $\alpha$ from 0.1 to 4. Our rod array is not a particularly good model for the non-fibrous materials used in the experiments, but our value of 0.25 for the dimensionless slip velocity corresponds to an $\alpha$ value of 4, which is at the edge of the experimental values.

## 4. Concluding remarks

The present work suggests that the Brinkman equation is not a good model for flow at the interface of a low-solidity porous medium, at least not for a medium composed of fibres oriented across the flow. The equation predicts a dimensionless slip velocity of 1, while we found that velocity to be around 0.3 over a wide range of conditions. Moreover, the Brinkman equation predicts that the outer flow penetrates the medium to a depth of $\sqrt{k}$ or to about half the distance to the second row in an array, while our results show very little penetration. Since our results are accurate to $O(\phi)$, it is concluded that the Brinkman model does not provide an accurate description of flow at the interface of an array or rods.

The most practical results of the present work are values of the slip velocity, for these values provide the second boundary condition for flow in a channel. The values are presented here in terms of a dimensionless slip velocity, and this quantity was found to be around 0.3 for shear-driven flows and to be less than that for pressure-driven flows, the difference depending on the physical situation. These values, contained in figures 7 to 9, should be useful in design situations where an estimate is wanted for the slip velocity in channel flow, when the channel is adjacent to a fibrous porous medium.

https://doi.org/10.1017/S0022112000002160 Published online by Cambridge University Press

The support of this work by the Natural Sciences and Engineering Research Council of Canada (NSERC) is gratefully acknowledged.

## REFERENCES

Beavers, G. S. & Joseph, D. D. 1967 Boundary conditions at a naturally permeable wall. *J. Fluid Mech.* **30**, 197–207.

Brinkman, H. C. 1947 A calculation of the viscous force exerted by a flowing fluid on a dense swarm of particles. *Appl. Sci. Res.* A **1**, 27–34.

Davis, A. M. J. 1993 Periodic blocking in parallel shear or channel flow at low Reynolds number. *Phys. Fluids* A **5**, 800–809.

Doyle, P. S., Shaqfeh, E. S. G. & Gast, A. P. 1998 Rheology of Polymer Brushes: A Brownian Motion Study. *Macromolecules* **31**, 5474–5486.

Howells, I. D. 1974 Drag due to the motion of a Newtonian fluid through a sparse random array of small rigid fixed objects. *J. Fluid Mech.* **64**, 449–475.

Jackson, G. W. & James, D. F. 1986 The permeability of fibrous porous media. *Can. J. Chem. Engng* **64**, 364–374.

Kim, S. & Russel, W. B. 1985 Modelling of porous media by renormalization of the Stokes equation. *J. Fluid Mech.* **154**, 269–286.

Larson, R. E. & Higdon, J. J. L. 1986 Microscopic flow near the surface of two-dimensional porous media. Part 1. Axial flow. *J. Fluid Mech.* **166**, 449–472.

Larson, R. E. & Higdon, J. J. L. 1987 Microscopic flow near the surface of two-dimensional porous media. Part 2. Transverse flow. *J. Fluid Mech.* **178**, 119–136.

Sangani, A. S. & Behl, S. 1989 The planar singular solutions of Stokes and Laplace equations and their application to transport processes near porous surfaces. *Phys. Fluids* A **1**, 21–37.

Sahraoui, M. & Kaviany, M. 1992 Slip and no-slip velocity boundary conditions at interface of porous, plain media. *Intl J. Heat Mass Transfer* **35**, 927–943.

Taylor, G. I. 1971 A model for the boundary condition of a porous material. Part 1. *J. Fluid Mech.* **49**, 319–326.

https://doi.org/10.1017/S0022112000002160 Published online by Cambridge University Press